https://ntrs.nasa.gov/search.jsp?R=20200001620 2020-03-28T19:11:44+00:00Z

NASA/TM—2020-220473 AIAA–2020–0545

Development of a Thermal Management System for Electrified Aircraft

Jeffryes W. Chapman, Sydney L. Schnulo, and Michael P. Nitzsche
Glenn Research Center, Cleveland, Ohio

March 2020

NASA STI Program . . . in Profile

Since its founding, NASA has been dedicated to the advancement of aeronautics and space science. The NASA Scientific and Technical Information (STI) Program plays a key part in helping NASA maintain this important role.

The NASA STI Program operates under the auspices of the Agency Chief Information Officer. It collects, organizes, provides for archiving, and disseminates NASA's STI. The NASA STI Program provides access to the NASA Technical Report Server—Registered (NTRS Reg) and NASA Technical Report Server—Public (NTRS) thus providing one of the largest collections of aeronautical and space science STI in the world. Results are published in both non-NASA channels and by NASA in the NASA STI Report Series, which includes the following report types:

- TECHNICAL PUBLICATION. Reports of completed research or a major significant phase of research that present the results of NASA programs and include extensive data or theoretical analysis. Includes compilations of significant scientific and technical data and information deemed to be of continuing reference value. NASA counter-part of peer-reviewed formal professional papers, but has less stringent limitations on manuscript length and extent of graphic presentations.

- TECHNICAL MEMORANDUM. Scientific and technical findings that are preliminary or of specialized interest, e.g., "quick-release" reports, working papers, and bibliographies that contain minimal annotation. Does not contain extensive analysis.

- CONTRACTOR REPORT. Scientific and technical findings by NASA-sponsored contractors and grantees.

- CONFERENCE PUBLICATION. Collected papers from scientific and technical conferences, symposia, seminars, or other meetings sponsored or co-sponsored by NASA.

- SPECIAL PUBLICATION. Scientific, technical, or historical information from NASA programs, projects, and missions, often concerned with subjects having substantial public interest.

- TECHNICAL TRANSLATION. English-language translations of foreign scientific and technical material pertinent to NASA's mission.

For more information about the NASA STI program, see the following:

- Access the NASA STI program home page at http://www.sti.nasa.gov

- E-mail your question to help@sti.nasa.gov

- Fax your question to the NASA STI Information Desk at 757-864-6500

- Telephone the NASA STI Information Desk at 757-864-9658

- Write to:
  NASA STI Program
  Mail Stop 148
  NASA Langley Research Center
  Hampton, VA 23681-2199

NASA/TM—2020-220473 AIAA–2020–0545

Development of a Thermal Management System for Electrified Aircraft

Jeffryes W. Chapman, Sydney L. Schnulo, and Michael P. Nitzsche
Glenn Research Center, Cleveland, Ohio

Prepared for the
AIAA SciTech Forum
sponsored by the American Institute of Aeronautics and Astronautics
Orlando, Florida, January 6–10, 2020

National Aeronautics and
Space Administration

Glenn Research Center
Cleveland, Ohio 44135

March 2020

Acknowledgments

The authors would like to thank the NASA Transformational Tools and Technologies (TTT) project and the Convergent Aeronautics Solutions (CAS), both under the Transformative Aeronautics Concept Program (TACP) for the funding of this work. The authors would also like to thank Justin Gray and Robert Falck of NASA Glenn Research Center for their aid with OpenMDAO and Dymos.

This report is a formal draft or working paper, intended to solicit comments and ideas from a technical peer group.

This report contains preliminary findings, subject to revision as analysis proceeds.

This work was sponsored by the Transformative Aeronautics Concepts Program.

Trade names and trademarks are used in this report for identification only. Their usage does not constitute an official endorsement, either expressed or implied, by the National Aeronautics and Space Administration.

Level of Review: This material has been technically reviewed by technical management.

Available from

NASA STI Program
Mail Stop 148
NASA Langley Research Center
Hampton, VA 23681-2199

National Technical Information Service
5285 Port Royal Road
Springfield, VA 22161
703-605-6000

This report is available in electronic form at http://www.sti.nasa.gov/ and http://ntrs.nasa.gov/

Development of a Thermal Management System for Electrified Aircraft

Jeffryes W. Chapman, Sydney L. Schnulo, and Michael P. Nitzsche*
National Aeronautics and Space Administration
Glenn Research Center
Cleveland, Ohio 44135

Abstract

This paper describes the development and optimization of a conceptual thermal management system for electrified aircraft. Here, a vertical takeoff and landing (VTOL) vehicle is analyzed with the following electrically sourced heat loads considered: motors, generators, rectifiers, and inverters. The vehicle will employ liquid-cooling techniques in order to acquire, transport, and reject waste heat from the vehicle. The purpose of this paper is to threefold: (1) Present a potential modeling framework for system level thermal management system simulation, (2) Analyze typical system characteristics, and (3) Perform optimization on a system developed for a specific vehicle to minimize weight gain, power utilization, and drag. Additionally, the paper will study the design process, specifically investigating the differences between steady state and transient sizing, comparing simulation techniques with a lower fidelity option and quantifying expected error.

Nomenclature

ACC	Air coolant cooler
A	Area
A_c	Exchanger minimum free-flow area
AU	Product of area and overall heat transfer coefficient
C	Capacity rate ($C_p * W$)
CR	Capacity rate ratio $\left(\frac{C_{\min}}{C_{\max}}\right)$
C_p	Specific heat at constant pressure
D	Diameter
$dPqP$	Change in pressure divided by pressure $\left(\frac{\Delta P}{P}\right)$
dT	difference in input temperatures for a 2-sided heat exchanger
f	Friction factor
G	Flow-stream mass velocity
h	Convection coefficient
HEx	Heat exchanger
ht	Height
K	Loss coefficient
k	Conduction coefficient
l	Length

*Lewis' Educational and Research Collaborative Internship Project (LeRCIP) student

m	Fin effectiveness parameter
MDAO	Multidisciplinary design analysis and optimization
Nu	Nusselt number
NTU	Number of heat transfer units
P	Pressure
Pwr	Power
Pr	Prandtl number
q	Heat transfer rate
q/dT	Heat rate divided by temperature difference
R	Specific gas constant
Re	Reynolds number
r_h	Hydraulic radius
SNOPT	Sparse Nonlinear OPTimizer
St	Stanton number
T	Temperature
th	Wall thickness
TMS	Thermal management system
U	Overall heat transfer coefficient
w	Width
W	Mass flow
Wt	Weight
Vol	Volume
VTOL	Vertical takeoff and landing
α	Ratio of total transfer area for one side of heat exchanger to total volume
δ	Fin thickness
ε	Effectiveness
η_o	Overall effectiveness
η_f	Fin effectiveness
μ	Dynamic viscosity
ρ	Density
σ	Ratio of free-flow area to frontal area

Subscripts:

c	Cold
h	Hot
fin	Fin
fr	Frontal
in	Input
m	Median
max	Maximum
min	Minimum
out	Output
th	Throat
w	Wall

I. Introduction

Thermal management on aircraft is becoming increasingly complex as onboard electrical needs have increased (Ref. 1). These increases have been in the form of more electrified aircraft and fully electric aircraft (Refs. 2 and 3) with estimated power requirements reaching megawatt levels (Ref. 4). Such high power systems generate large heat loads that must be rejected in order to preserve system and component integrity. It is imperative, therefore, that effective and robust thermal management systems (TMS) be designed. These systems can employ multiple cooling methods, such as passive heat sinks, liquid and spray cooling, and active cooling with heat pumps (Refs. 5 to 7). This paper will analyze liquid cooling strategies optimized to minimize system power requirements, weight, and aerodynamic effect. The methods within this paper, while general, have been used within multidisciplinary optimization research of aircraft propulsion systems (Refs. 8 to 10). The focus of the TMS within this paper is to cool the electric devices of the aircraft, which is typically done using liquid-cooling strategies. As a result, a liquid-cooled system will be analyzed and used to provide a good starting point for future cooling system comparisons and trade studies (Ref. 11).

Liquid-cooled systems consist of a transfer fluid (called a "coolant") that acquires and transports energy from heat-generating devices to a heat exchanger for subsequent rejection. In aircraft, an Air-to-Coolant Cooler (ACC) type heat exchanger (HEx) is typically employed where the air either supplied by aircraft ram air or by a specifically-designed puller fan. The TMS is designed to cool components to required temperature limits while also minimizing weight, power usage, and drag. Common system-level design parameters include: HEx dimensions, HEx type, amount of cooling flow, size of coolant plumbing, exit throat area for air cooling flow, coolant pump sizes, puller fan (if required) sizes, and system arrangement. Since many of these design parameters are dependent on each other, an optimizer must be used to size the heat exchangers. For systems like this one, design is routinely conducted using steady-state analysis; however, for aviation purposes, where the mission phases are short relative to thermal transients, the design process may require the consideration of transient operation in order to reduce weight, drag, and/or system power use.

Two systems will be analyzed in this paper. First, a simple TMS loop consisting of a load, and a heat exchanger is explored to understand the relationship between the design criteria, cooling operation, and TMS power usage. This simple system will subsequently be used for three additional studies: a comparison of modeling techniques to compare the HEx modeling proposed within this paper to a simple map-based method, a system transient sensitivity study, and an optimization study. The second test case for this study will be a TMS designed for a 15-passenger turboelectric tiltwing vertical takeoff and landing (VTOL) vehicle, developed as an urban taxi concept vehicle by NASA (Figure 1) (Ref. 12). The design mission for this vehicle includes vertical takeoff, hover, fly 50 nm, hover, and land. This series would be completed eight times before refueling, for a total of a 400 nm range. The power plant consists of a single turboshaft engine driving a generator that subsequently powers four 730 hp electric motors. Electric components for the propulsion system include a generator, rectifier, battery (for emergency only), four inverters, and four electric motors. To maintain generality with all electric aircraft, waste heat will be rejected to an air stream independent of the turboshaft. The design of the TMS will consider the typical mission profile and examine the transient heat loads using lump system masses. It should be noted that this study designs the system to meet the thermal requirements for only this mission. Therefore, because the battery will not be used for a typical mission, it has been neglected. It should be noted that similar studies detailing the design of a TMS for conventional takeoff and landing vehicles utilizing EAP were performed by United Technologies Research (Refs. 11 and 13).

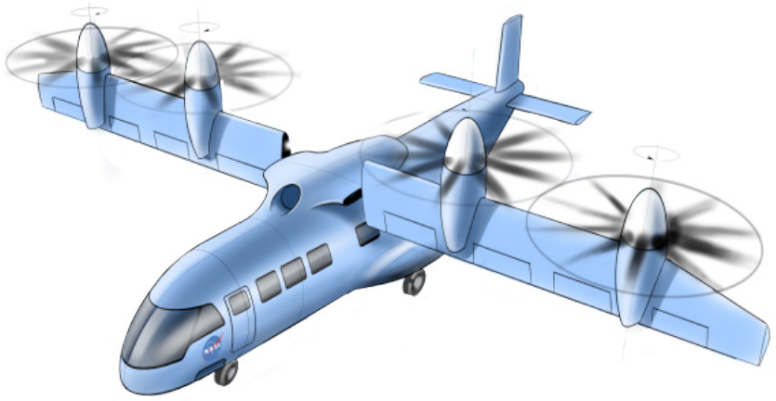

Figure 1.—Tiltwing vehicle utilizing turboelectric propulsion (Ref. 12).

All thermal modeling in this paper has been conducted with the OpenMDAO framework. OpenMDAO is an open source package built to perform multidisciplinary design analysis and optimization (MDAO) within the python language (Ref. 14). OpenMDAO provides sets of solver and optimizer tools as well as a python development framework that is leveraged to perform TMS optimization. The specific optimizer used for the work was the Sparse Nonlinear OPTimizer (SNOPT) (Ref. 15). Evaluation of the dynamic system was performed using the OpenMDAO add on Dymos that enables transient optimization (Ref. 16).

Subsequent sections of this paper detail the engine design and optimization study. Specifically, a detailed description of thermal code development will be given in Section II, followed by an analysis of a single load single heat exchanger model in Section III. A detailed discussion of the design and optimization of the TMS system for a tiltwing vehicle will be given in Section IV. Finally, the summary will be given in Section V.

II. Thermal Management System Code Development

This paper explores the relationship between the TMS and aircraft performance. For this purpose, the code development within this section determines system weight, drag, and power usage based on the required heat rejection. A liquid cooling system is comprised of components that reject heat to a coolant fluid, typically engine oil, engine fuel, or some type of coolant. This fluid then transports the heat to a heat exchanger that rejects the energy to another fluid for aircraft removal or storage, typically air or engine fuel. Engine fuel will not be considered within this paper, however the equations and methodology laid out would be compatible with its use. Three major References (17 to 19) were used in the development of this paper's thermal management software.

There are two main components employed in our TMS architecture: the cold plate and the heat exchanger. A cold plate (single flow heat exchanger or a heat sink) is defined, for this paper, as a device that uses liquid to cool a heat source or moves heat from a heat source to a fluid, such as electronics designed with fluid passages meant to remove the heat. A heat exchanger is defined as a device that moves heat from one fluid to another fluid. Each heat exchanger for this project will be assumed to be plate type. Thermal and transport properties are computed using the PyCycle package, (Ref. 20) the open source package cool prop, (Ref. 21) and/or via table lookups based on technical data sheets (aircraft coolant, (Ref. 22) or (Ref. 23), or aircraft fuel, (Ref. 24)).

The following sub-sections define the theory employed in the model development, with sub-section A detailing heat exchanger performance, B showing coolant line performance, C demonstrating how system drag/thrust was calculated, D showing the weight calculation for each component, and E tabulating the power required to operate the system.

A. Heat Exchanger Performance

Each heat exchanger is defined by a block size (width (w), length (l), and height (ht)) and each flow surface/side is defined by the ratio of free-flow to frontal area (σ), the ratio of total heat transfer area to the total volume (α), hydraulic radius (r_h), and heat capacity rate (C). These relations are shown in Equations (1) and (2), where A_c is free-flow area of the surface, A_{fr} is frontal area of the surface, A_{th} is the thermal transfer area of the surface, C_p is the specific heat, G is the flow mass velocity, and Vol is volume.

$$\begin{aligned} Vol &= w * l * ht \\ A_{fr} &= w * ht \\ \sigma &= \frac{A_c}{A_{fr}} \\ \alpha &= \frac{A_{th}}{Vol} \end{aligned} \tag{1}$$

$$\begin{aligned} r_h &= \frac{\sigma}{\alpha} \\ C &= W * C_p \end{aligned} \tag{2}$$

After defining the physical parameters of the component, the flow can be characterized by calculating the Reynolds number (Re) as detailed in Equation (3), where μ is the dynamic viscosity.

$$\begin{aligned} G &= \frac{W}{A_{fr}\sigma} \\ \mathrm{Re} &= \frac{4 r_h G}{\mu} \end{aligned} \tag{3}$$

Once the Reynolds number has been determined, it can be applied to a series of empirical relationships to determine friction factor (f) for calculating flow pressure drop and Stanton number (St) or Nusselt number (Nu) for calculating the convection coefficient of heat transfer (h). For this development the cold plate is assumed to be a pipe and utilizes the Nusselt number calculations for a tube, while heat exchanger relationships are taken from Kays and London. It should be noted that flow may affect the equations utilized. For this paper, the flow will be considered to be laminar if Re is less than 2000 and turbulent if it is greater than 2000. These break points are not exact, as the transition from laminar to turbulent flow is not binary, however for the purposes of this modeling effort they are satisfactory. The flow equations used in the code are shown in Equations (4) to (6), where Pr is the Prandtl number, $f()$ means an empirical function of (or table lookup), and k is thermal conductivity.

$$\mathrm{Pr} = \frac{\mu C_p}{k} \tag{4}$$

For laminar flow through a tube assuming uniform surface temperature:

$$\mathrm{Nu} = 3.66$$
$$f = 64 * \mathrm{Re}^{-1}$$

For fully developed turbulent flow through a tube:

$$\mathrm{Nu} = 0.023 * \mathrm{Re}^{0.8} * \mathrm{Pr}^{0.4}, \text{ Dittus-Boelter equation} \tag{5}$$
$$f = 0.046 * \mathrm{Re}^{-0.02}$$

$$h = \frac{\mathrm{Nu} * k}{4 * r_h}$$

or, for heat exchanger surfaces

$$\mathrm{St} * \mathrm{Pr}^{\frac{2}{3}} = \mathrm{f(Re)}$$
$$f = \mathrm{f(Re)} \tag{6}$$
$$h = \mathrm{St} * G * C_p$$

For heat exchangers with extended surfaces, fin effectiveness and overall effectiveness should also be calculated. This effectiveness modification takes into account the reduction of performance due to temperature gradients along the extended surface. These equations are shown in Equation (7), where m is the fin effectiveness parameter, δ is the fin thickness, k is the conduction coefficient, A_{fin} is the fin area for the surface, η_f is fin effectiveness, and η_o is overall effectiveness. From the equation it can be noticed that if there are no fins on a surface, η_o is unity.

$$m = \sqrt{\frac{2h}{k\delta}}, \text{ for thin sheet fins}$$
$$\eta_f = \frac{\tanh(ml)}{ml} \tag{7}$$
$$\eta_o = 1 - \frac{A_{\mathrm{fin}}}{A_{th}}\left(1 - \eta_f\right)$$

Each of the above equations are solved for each surface of the heat exchanger. In most cases, there is one surface (cold plate or heat sink) or two surfaces (heat exchanger). The thermal exchange between the two fluids may be represented by a thermal network consisting of each heat exchanger component. In the case of a 2 flow heat exchanger, the thermal network may be represented by a convective surface, a wall, and another convective surface, as shown in Figure 2. To determine the overall conductance for a surface, the thermal network resistances may be combined as shown in Equation (8), where U is overall heat transfer coefficient based on a per unit area of a particular surface, th is wall thickness. Subscript h is for the hot side, c is for the cold side, and w is for wall. Note, only equations for the hot side are shown. The cold side equations may be derived by reversing the hot and cold variables. Assuming the wall resistance is negligible and simplifying further, Equation (9) may be used to obtain the hot side U.

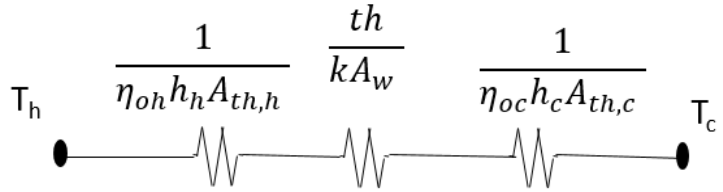

Figure 2.—Thermal network for a heat exchanger (note, *A* is thermal area).

$$\frac{1}{U_h} = \frac{1}{\eta_{oh} h_h} + \frac{th}{k \frac{A_{th,w}}{A_{th,h}}} + \frac{1}{\eta_{oc} h_c \frac{A_{th,c}}{A_{th,h}}} \tag{8}$$

$$\frac{1}{U_h} = \frac{1}{\eta_{oh} h_h} + \frac{1}{\eta_{oc} h_c \frac{\alpha_c}{\alpha_h}} \tag{9}$$

Once *U* is calculated the heat exchanger effectiveness (ε) can be determined. This paper will make use of the Number of Transfer Units (NTU) method, which explores the relationship between NTU (Eq. (10), where $C_{\min}$ is the minimum all heat capacity rates) and heat exchanger effectiveness. This relationship changes based on the heat exchanger type. Effectiveness equations for cold plate and cross flow are shown in Equation (11), where CR is heat capacitance ratio ($C_{\min}/C_{\max}$). It should be noted that the definition for the cold plate is based on the assumption that the C_p of the heat source is infinite.

$$\mathrm{NTU} = \frac{\mathrm{UA}_{th}}{C_{\min}} \tag{10}$$

For cold plate or heat sink:

$$\epsilon = 1 - \exp(-\mathrm{NTU})$$

For cross-flow heat exchanger: (11)

$$\epsilon = 1 - \exp\left[\left(\frac{1}{\mathrm{CR}}\right) \mathrm{NTU}^{0.22} \{\exp[-\mathrm{CR} * \mathrm{NTU}^{0.78}] - 1\}\right]$$

Maximum energy transfer is then calculated and the heat exchanger effectiveness is applied to determine the actual energy transferred. Exit temperatures can be calculated based on the energy balance, as shown in Equation (12).

$$\begin{gathered} q_{\max} = C_{\min}\left(T_{h,\mathrm{in}} - T_{c,\mathrm{in}}\right) \\ q = \epsilon * q_{\max} \\ q = C_c\left(T_{c,\mathrm{out}} - T_{c,\mathrm{in}}\right) = C_h\left(T_{h,\mathrm{in}} - T_{h,\mathrm{out}}\right) \end{gathered} \tag{12}$$

To fully define the heat exchanger flow, the pressure must also be calculated. For any given surface, the equation for the pressure drop is shown in Equation (13), where ρ is density, *K* is a loss coefficient, and subscripts in and out stand for the flow at the input and exit of the heat exchanger, respectively, and m stands for mean. It should be noted that the ρ_m equation assumes density adjusts fairly linearly with respect to temperature. If density does not behave linearly with the chosen fluid, then the ρ_m equation should be adjusted accordingly. *K* factors within the equation are typically within the range of ±1 and can be determined based on σ, Re, and surface type. In this study they are assumed to be constant and consistent with typical operating values as shown in Kays and London. Additionally, in systems where the flow is uncompressible, the equation simplifies, as shown in Equation (14).

$$\rho_m = \frac{\rho_{\text{in}} + \rho_{\text{out}}}{2}$$

$$\frac{\Delta P}{P_{\text{in}}} = \frac{G^2}{2\rho_{\text{in}} P_{\text{in}}}\left[(K_{\text{in}} + 1 - \sigma^2) + 2\left(\frac{\rho_{\text{in}}}{\rho_{\text{out}}} - 1\right) + f\frac{l}{r_h}\frac{\rho_{\text{in}}}{\rho_m} - (1 - \sigma^2 - K_{\text{out}})\frac{\rho_{\text{in}}}{\rho_{\text{out}}}\right] \tag{13}$$

when $\rho = \rho_{\text{in}} = \rho_{\text{out}}$:

$$\frac{\Delta P}{P_{\text{in}}} = \frac{G^2}{2\rho P_{\text{in}}}\left[(K_{\text{in}} + 1 - \sigma^2) + f\frac{l}{r_h} - (1 - \sigma^2 - K_{\text{out}})\right] \tag{14}$$

B. Coolant Line Thermal Performance

Coolant lines act to transport the thermal energy to the heat exchanger for removal from the aircraft. Performance for the coolant lines was determined in a simplified and conservative manner. Pressure drop for each coolant line was calculated based on a constant percentage of pressure loss set to 1 percent. Heat loss within the coolant lines was neglected. Line fidelity could be increased by developing a line thermal transfer relationship based on length of line and surrounding temperature. Line pressure loss is set in accordance with the line diameter design as shown in Equation (17).

C. Drag/Thrust

Overall system drag is calculated using a thermodynamic approach and is considered when air is drawn into a heat exchanger and then exits after heat is rejected. In this case, the architecture includes an inlet in line with a heat exchanger (adding heat and removing pressure from the flow), followed by a puller fan (if needed), and an exit nozzle, as shown in Figure 3. This configuration is convenient because it allows for cooling capability when ram air is negligible.

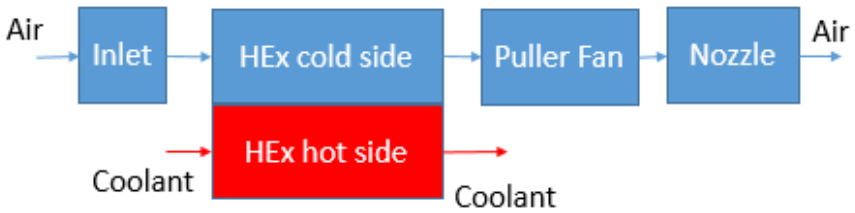

Figure 3.—Example air ducting for heat exchanger.

The inlet for this example is modeled as a pressure drop of 1 percent. It was determined that this number would be updated as more information about the geometry of the inlet was developed and a high-fidelity analysis could be performed. The heat exchanger pressure drop and change in temperature are estimated based on the equations earlier in the paper. A puller fan may be added after the heat exchanger when the pressure drop is too great or if the system will need to be cooled at stationary conditions when ram air is not available. The modeling of this puller fan makes use of isentropic relations and assumes the fan runs fast enough to generate an exit pressure equal to 1 percent greater than ambient pressure, but only when the pressure after the HEx is less than that limit. This assumption allows the model to successfully operate at off nominal points without the possibility of a backflow calculation. The nozzle is represented by an ideal throat calculation. This calculation determines the flow for the duct system based on a select nozzle throat area. Thrust for the thermal system is then calculated utilizing the mass flow and velocity for the incoming and exiting air streams. Details about the nozzle model and drag calculation are found in Reference 25.

D. Weight

The system weight is determined by considering each component accordingly. The contributions due to the inlet, heat exchanger housing, heat exchanger header, and nozzle have been neglected initially due to the specialized nature of their geometries and the assumption they would scale as heat exchanger core weight scaled (which was deemed acceptable at this stage of the design). The cold plate weight has also been neglected because it was assumed its mass contribution would be integrated with the device to be cooled.

Heat exchanger weight is calculated by area as shown in Equation (15). In this equation, the total volume is calculated and the open space is removed for the dry heat exchanger. Coolant weight is then added back in via the wet equation.

$$\begin{aligned} Wt_{\mathrm{HEx,dry}} &= (A_{fr,c}(1-\sigma_c) * l_c \; - \; \sigma_h * A_{fr,h} * l_h) * \rho_{\mathrm{aluminum}} \\ Wt_{\mathrm{HEx,wet}} &= Wt_{\mathrm{HEx,dry}} + \; A_{fr,c} * \sigma_c * l_c * \rho_c + A_{fr,h} * \sigma_h * l_h * \rho_h \end{aligned} \tag{15}$$

Coolant line weight is calculated using the diameter of the line and the length, as shown in Equation (16), where *D* is the diameter of the coolant line. The diameter is found using a design pressure drop of 1 percent and the Darcy-Weisbach formulation for laminar flow through a pipe, which is in Equation (17).

$$Wt_{\mathrm{coolant\,line}} = 0.25 * \pi * l_{\mathrm{coolant\,line}} * D^2 * \rho_{\mathrm{coolant}} \tag{16}$$

$$\Delta P_{\mathrm{coolant\,line}} = \frac{128 * l_{\mathrm{coolant}} * \mu_{\mathrm{coolant}} * W_{\mathrm{coolant}}}{\pi * \rho_{\mathrm{coolant}} * D^4} \tag{17}$$

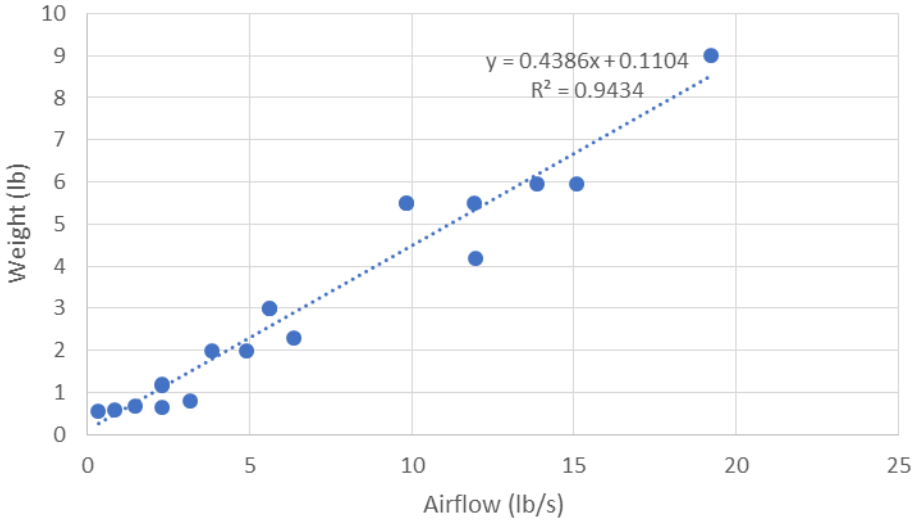

Figure 4.—Puller fan weight correlation.

Fan and pump weight were empirically derived as function of mass flow. For the pump, a displacement is determined and then used to generate a weight, as shown in Equation (18) (Ref. 26), where W is in lbm/s, ρ is in lbm/in.^{3}, pump displacement is in in.^{3}/rev, and Wt is weight in lbm.

$$\text{Pump Displacement} = 0.0092 * \left(\frac{W_{\text{coolant}}}{\rho_{\text{coolant}}}\right)^{1.3857}$$
$$Wt_{\text{pump}} = 8.5942 * \text{Pump Displacement} + 2.4229 \tag{18}$$

Puller fan weight was determined using a cooler fan weight correlation based on mass flow, which is shown in Figure 4 and Equation (19). In these correlations, where W is in lbm/s and Wt is in lbm. Data for the correlation was taken from manufacturer specification sheets from Lytron, and Orientalmotor MRS Series and MU Series axial cooling fans.

$$Wt_{\text{puller fan}} = 0.4386 * W_{\text{air}} + 0.1104 \tag{19}$$

E. Power

Both the TMS pumps and puller fans require power to run. The power required to operate the pumps, as shown in Equation (20), depends on the pressure drop and flow rate within a coolant loop (Ref. 19).

$$\text{Power}_{\text{pump}} = \frac{W * \Delta P}{\rho^2} \tag{20}$$

Puller fan power is calculated based on the thermodynamic power increase in the fluid as shown in Equation (21), where T is temperature with output temperature taking into account the efficiency of the fan.

$$\text{Power}_{\text{puller fan}} = W * Cp * (T_{\text{out}} - T_{\text{in}}), \text{ for air flow} \tag{21}$$

III. Simple Heat Exchanger Circuit Analysis

To gain an understanding of general TMS transient behavior, a simple heat exchanger circuit was set up. A block diagram of this system is shown in Figure 5. In this system, a heat transfer fluid flows through a cold plate where it picks up heat. This transfer fluid then flows through the cold side of the heat exchanger to shed the heat it gained from the cold plate. Afterwards, the fluid returns to the cold plate to acquire additional energy.

For transient analysis, the cold plate is assumed to be attached to a lump mass heat load and a reservoir of cooling fluid is added just before entry into the cold plate. These elements were set as stand-ins for any mass or fluid state that would be required for the system. In this model, the cooling fluid was assumed to be air and transfer fluid was selected to be either water, oil, or propylene glycol 30 percent.

The following sub-sections will be discussed: A, a steady state analysis of a fixed heat exchanger design, along with a comparison of the proposed model with that of a simple map based model; B, a transient analysis of a fixed heat exchanger design; and C, a study of optimized heat exchanger designs. Sizing characteristics for steady state and transient simulations were set to constants, with load weight and reservoir fluid weight adjusted separately. For optimization runs, sizing characteristics were allowed to change to meet a set objective.

A. Steady-State Heat Exchanger Analysis

A steady state model of a simple HEx system, shown in Figure 5, was developed and a sensitivity study was performed on the heat exchanger. Heat exchanger size parameters were optimized for a specific design point. Heat exchanger input temperatures and fluid mass flows were adjusted and analyzed for sensitivity. Performance behavior are obtained for q/dT (rejected power divided by the difference in input temperatures), AU or UA_{th}, and ε. Additionally, a comparison demonstrates the effects of neglecting absolute input temperatures, and only considers the difference in temperature between the hot and cold side inputs. The purpose of this exercise is to show how HEx performance changes with input parameters and demonstrate potential error when utilizing performance maps only considers a subset of the inputs. It should be noted that performance shifts for changes in input pressure were assumed to be negligible for uncompressible fluids (oil, water, and propylene glycol 30 percent). Additionally, an input pressure sensitivity study was conducted for air.

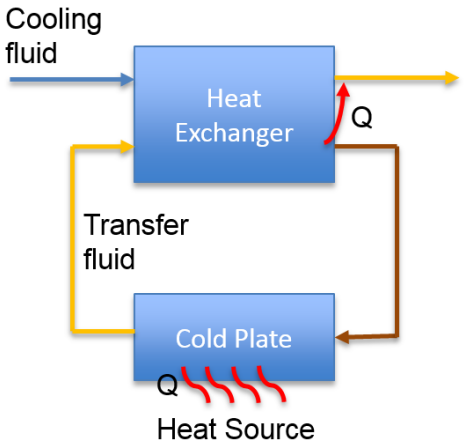

Figure 5.—Simple heat exchanger system.

Initial sizing of the system was performed to reject 50 kW of power from a plate fin type HEx (shown in Figure 6, where b is the plate spacing) using propylene glycol water 30 percent (aircraft coolant) as the transfer fluid and air as the cooling fluid. Heat exchanger input temperatures at the design point were 317 and 380 K for the cooling fluid and transfer fluid, respectively. Additional HEx parameters include a volume of 0.005 m^3, weight of 8.5 kg, an effectiveness of 0.84, input air mass flow of 2.15 kg/s, and input propylene glycol 30 percent mass flow of 0.22 kg/s at the design point. Off-design, input mass flows were adjusted from 0.5 to 8.0 kg/s for air and 0.1 to 1.0 kg/s for propylene glycol water 30 percent. Load weight and reservoir size were neglected for the steady-state runs.

The changes in performance due to off-design mass flows are shown in Figure 7, with the inflow temperatures set to the design values. In the graph it can be noted that AU, q, and q/dT each contain the largest values when both flows are at their max values and taper off as either is reduced. Effectiveness has larger values as one flow is reduced and the other is increased. This form can also be seen in the traces of NTU and CR. It can be seen that the highest values of CR are at the low points of effectiveness and NTU, meaning that low efficiency is maintained when C_{min} is nearly the same value as C_{max}. Conversely, high effectiveness can be maintained when one C value dominates the other (with $C_{air} > C_{coolant}$ in the lower right and $C_{air} < C_{coolant}$ in the upper right), which can be achieved by increasing mass flow to a selected side of the heat exchanger. Looking at AU, q and dT, it can be seen that the cross over region of the effectiveness contour also marks a shift in mass flow dependence. For example, if W_coolant is 0.8 kg/s and W_air is 1 kg/s, little increase in q can be utilized by further increasing W_coolant, however increasing W_air will have a large benefit to rejected power by increasing the C_{min}. Exit pressures for each HEx side demonstrate a roughly second order drop off with increasing mass flow due to larger amounts of flow moving through an orifice of a constant size, as shown in Figure 8.

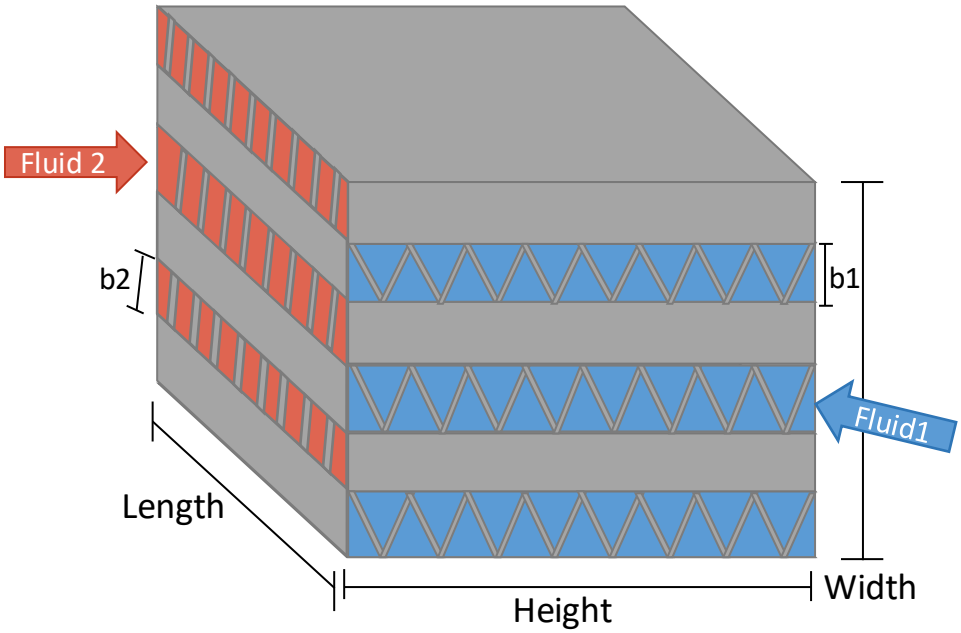

Figure 6.—Plate fin heat exchanger geometry.

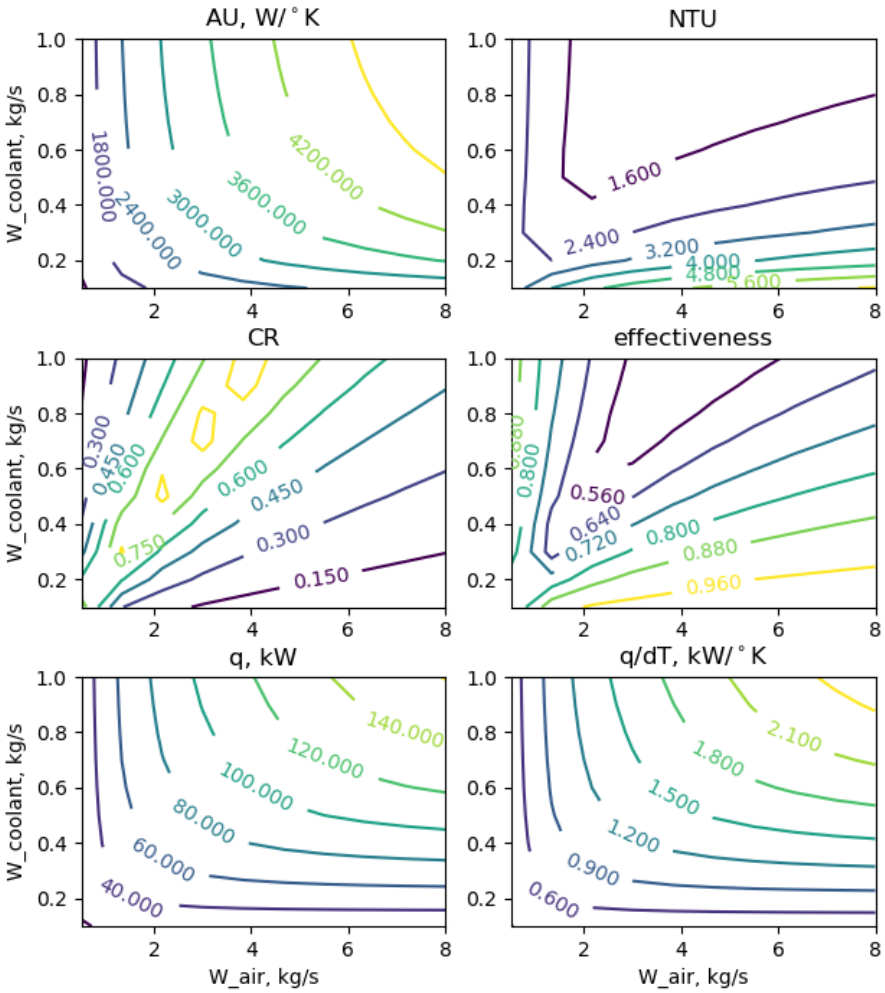

Figure 7.—Heat exchanger performance as function of input mass flow, at design temperatures and using propylene glycol water 30 percent as a coolant.

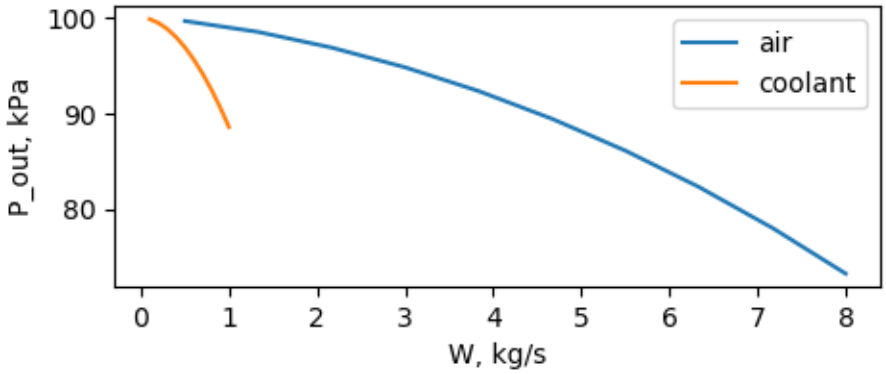

Figure 8.—Heat exchanger pressure as function of input mass flow, at design temperatures and using propylene glycol water 30 percent as a coolant.

Changes in HEx performance due to changes in input temperature can be seen in Figure 9, with mass flows set to design values. For each case, the values mark normalized difference from design point. Looking at the values in q, it can be seen that large (over 100 percent) differences are accrued as the ratio between the inlet temperatures is changed. Differences in CR are fairly low, with maximum values less than 1 percent. Differences in AU, NTU, effectiveness, and q/dT with maximum differences of roughly 25, 20, 5, and 8 percent, respectively. These differences show that off design temperatures result in fairly large differences for AU and NTU, however these differences do not result in large differences in effectiveness and q/dT. Additionally, it can be seen that large differences in q with changes in temperature can be reduced substantially (but not totally removed) by normalizing the q with respect with the change in temperature (q/dT). In summary, these show that a HEx performance is not only based on the difference in temperature between the two inputs, but also the absolute value of each input. Changes in pressure show very little dependence on temperature with a 0.8 and 0.3 percent difference on the air side and coolant side respectively.

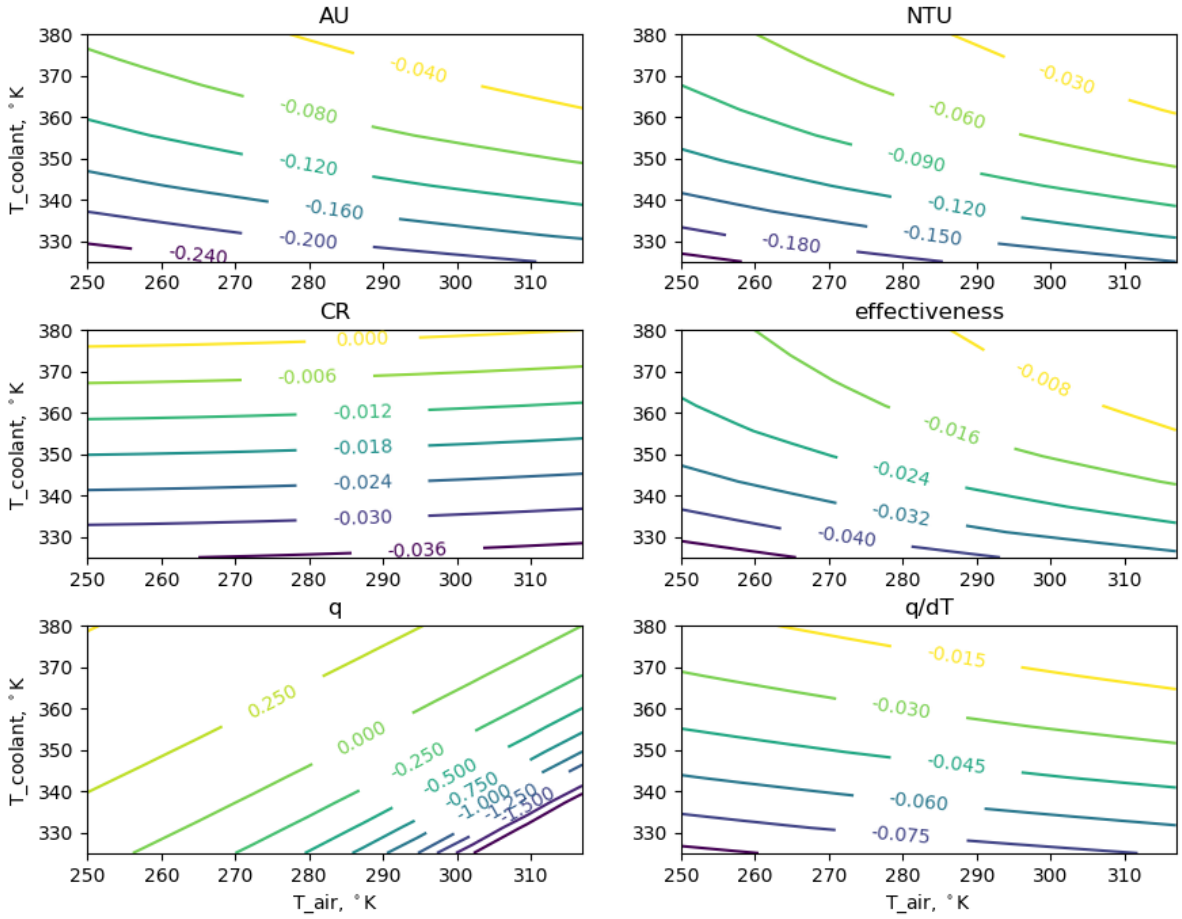

Figure 9.—Normalized delta heat exchanger performance as function of input temperature, at a 50 kW design point, design mass flows, and using propylene glycol water 30 percent as a coolant.

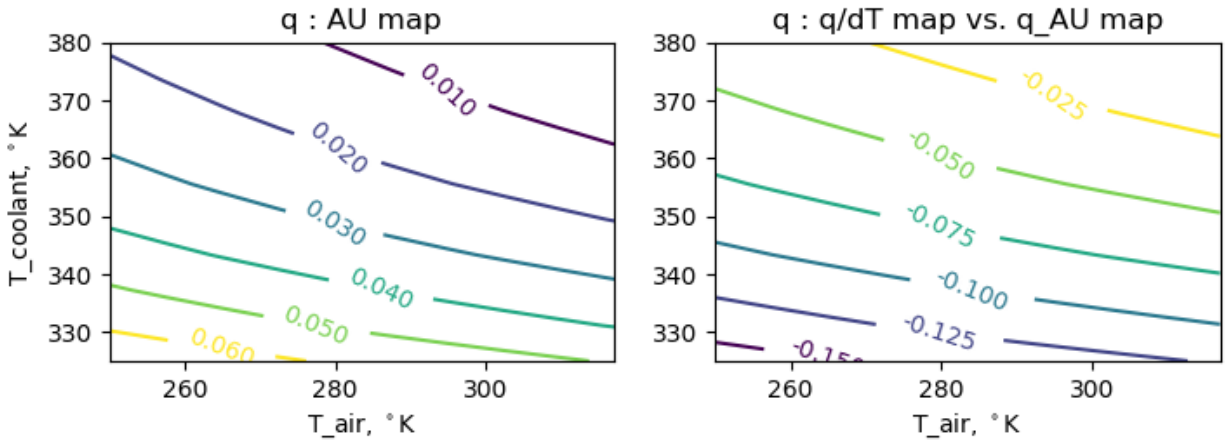

Figure 10.—Difference in q from the higher fidelity model compared with q calculated using an AU map and a comparison of q/dT map and AC map differences.

With this data, a comparison was completed to determine the differences between the modeling method proposed in this paper (higher fidelity method) and a simpler HEx map method. This study will examine a potential mass flow to q/dT or AU map. To gain a fair comparison between the two concepts, AU and q/dT data taken from the parameter study was used to replace the higher fidelity equations (see Eqs. (10) to (12)) and a final q was calculated. Running at off-design mass flow values shows both maps result in q values that are identical to the higher fidelity model, as the map is directly dependent on the input flows. Running with off-design temperatures show that utilizing a q/dT map to calculate q result in identical differences to those observed in Figure 9. Data from using the AU map and the comparison with the q/dT map derived q is shown in Figure 10. Looking at the AU map developed q, the maximum difference within the considered range is roughly 6 percent. Comparison between the two maps shows differences slightly higher with the q/dT map, with the majority of the difference coming from changes in coolant temperature. It should be noted that the difference between the two maps reaches a maximum of 15 percent.

The 50 kW HEx simulations above were also run using water and oil as the coolant type. With water, similar results (slightly higher q/dT) were observed at the given mass flows which is due to the similar specific heat values of water and propylene glycol water 30 percent. Temperature dependence was weaker with water relative to the propylene glycol water 30 percent, with maximum differences of roughly 4 percent in q/dT using water. For oil the operational temperatures were increased to 422 K. This increase in operational temperature caused q to increase, however, AU and q/dT were reduced by roughly half which led to a reduction in overall q. Additionally, temperature shifts in oil resulted in large changes in the HEx performance, as shown in Figure 19 in the Appendix, with differences of over 150, 60, and 75 percent for AU, effectiveness, and q/dT respectively. These demonstrate the importance of accounting for off-nominal coolant input temperatures in HEx systems using oil.

To gain an understanding of how differently sized HEx compare with the 50 kW HEx considered up until this point, a 150 kW HEx was developed. Optimizing the 150 kW system resulted in a HEx with a volume of 0.016 m^3, weight of 8.5 kg, an effectiveness of 0.84, input air mass flow of 6.4 kg/s, and input propylene glycol water 30 percent mass flow of 0.69 kg/s. Input mass flows were then adjusted from 0.5 to 8.0 kg/s for air and 0.1 to 1.0 kg/s for propylene glycol 30 percent. Contours with this new configuration can be seen in Figure 20 and Figure 21 in the Appendix. Comparing with the 50 kW version, it can be noticed that performance change with temperature are essentially the same. This is because fluid properties do not change with increasing load. The value of AU is roughly two times as

large due to the larger areas. Effectiveness shifts somewhat to the upper left allowing higher values at the larger flow values. Values of q/dT are slightly larger than those observed with in the 50 kW version and output pressures are similar for the coolant, but much less for air at the higher mass flow values. Overall, the larger heat exchanger has been resized mainly to increase the effectiveness and reduce pressure losses at the design mass flow ratios.

In addition to temperature, a study of pressure sensitivity was performed on air. This study was not extended to oil, water, or propylene glycol water 30 percent because they are noncompressible fluids. To perform the study, the model was set up to run in two different configurations, explicit and implicit. For the explicit case, input flow parameters were used in calculating exit pressure. On the other hand, the implicit case uses the average of the input and output pressures to iteratively calculate the output pressure. The simulations ran at initial pressures of 50, 100, and 200 kPa and the results of these runs are shown in Figure 11. In this figure it is seen that pressure drop is independent of starting pressure, however, at high pressure loss values (30 percent) the relative difference between the explicit and implicit methods reaches roughly 18 percent. This is because air density is a first order function of pressure according to the ideal gas law, therefore, the pressure drop is a function of only the pressure difference. In an attempt to reduce the simulation's dependence on pressure drop, a correction factor was developed (as shown in Eq. (22) and applied in Figure 11). This correction factor reduces error to below 2 percent for pressure drops less than 30 percent, which was deemed acceptable by the authors for a concept model.

$$\left(\frac{\Delta P}{P_{\text{in}}}\right)_{\text{corrected}} = \left(\frac{\Delta P}{P_{\text{in}}}\right)_{\text{uncorrected}} * \left(1 + \left(\frac{\Delta P}{P_{\text{in}}}\right)_{\text{uncorrected}}\right) \tag{22}$$

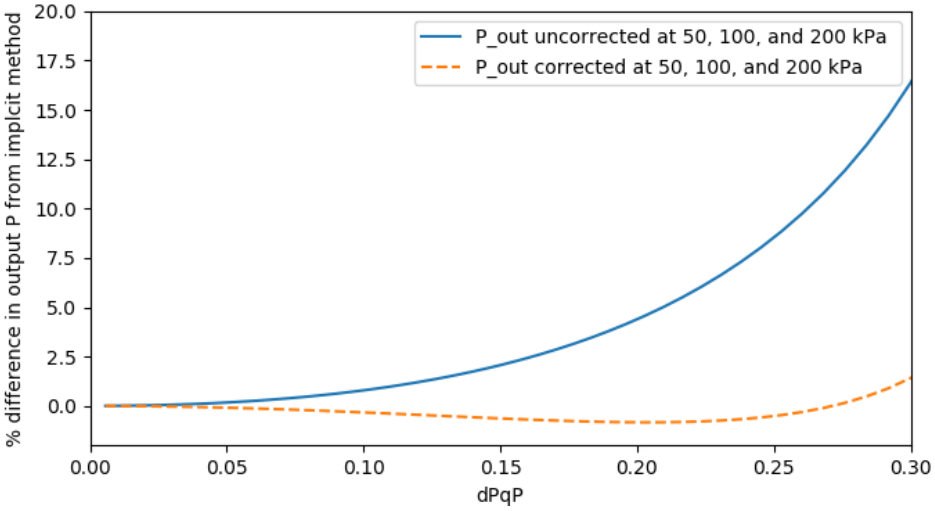

Figure 11.—Percent difference in calculated output pressure, implicit vs. corrected and uncorrected calculation method.

B. Transient Heat Exchanger Analysis

Transient capability was added into the system by adding two temperature states: a lump mass onto the load heat source, and a transfer fluid reservoir on the transfer fluid line before the load cold plate. These are considered general and could also take the form of any fluid or load state within the system. The purpose of this study is to analyze the system sensitivity these transient states and how the overall system response is affected by changes in the state's time constant. Traces of the system using water as a transfer fluid are shown in Figure 12. In this transient analysis, initial temperatures of the load and transfer fluid were set to 318 K. At 0 s, a 50 kW heat load is applied to the system and at 7000 s the load is reduced to 25 kW. Load and water weight were varied from 500 to 10 kg. In each case the temperature rises as the load is applied and then falls when the load is decreased with no overshoot in any case. When load weight is kept constant (500 kg), temperature settling time is decreased as water weight is reduced. All load temperatures reach within 5 degrees of final temperature within 1000 s. Water temperatures show a much larger spread with settling times of the low fluid reservoir weight system at around 1000 s and the highest weight settling near the 7000 s mark. With constant water weight and a varied load weight, water temperature settling times can be seen to remain fairly constant. For load temperature, there are two distinct phases during the transient. In the first phase, the transient is governed by the load weight and in the second phase it is governed by the water weight. This effect is most easily observed for the 10 kg load weight case, where the temperature rises very quickly during phase one and then rises much more slowly during phase two. In each of the traces in Figure 12, it could be said that the system would benefit from a transient design if responses have not reached steady state by the time the operating conditions change. For example, if this system were to operate at 100 percent power for only 2 min before transitioning to a lower power level, a steady-state design may be overly conservative.

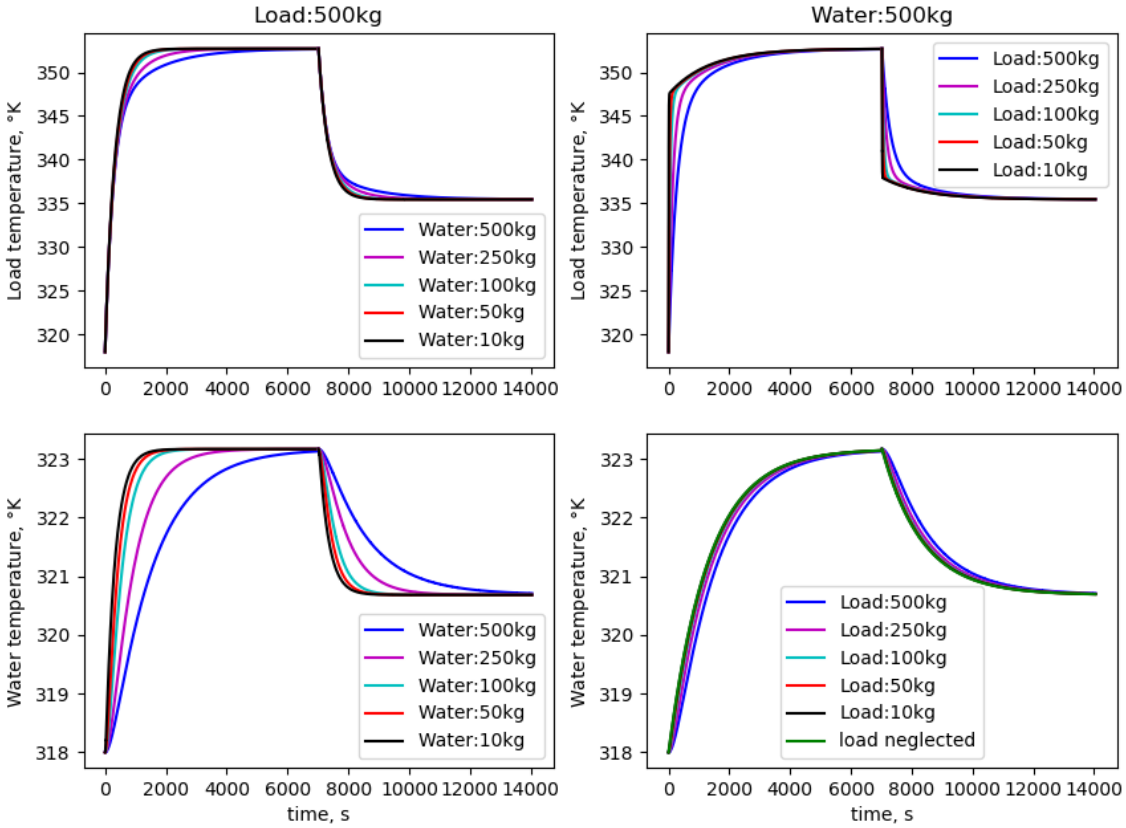

Figure 12.—Load and water temperature with varying load and water weight.

C. Heat Exchanger Optimization

In previous sub-sections, set heat exchanger geometries were considered at a number of operating conditions. This sub-section will discuss the optimization of these heat exchanger designs and will consider steady-state operation only. A diagram of the system model is located in Figure 5. The objective for the optimization is to reject a certain amount of power, while minimizing weight, power usage, and drag. Contributions to each of these include:

1. Weight
   a. heat exchanger
   b. fluid line coolant
   c. puller fan
   d. fluid pump
2. Power usage
   a. fluid pump
   b. puller fan
3. Drag
   a. inlet (drag)
   b. nozzle exit (thrust)

It should be noted that for this analysis the inlet, nozzle exit, coolant line nonfluid material, load header, and heat exchanger header weights were neglected. While these would increase the weight, the major contributors are considered, and it is therefore assumed that trends produced by the optimization would be sufficiently accurate for a conceptual design.

Development of the heat exchanger simulations was completed with OpenMDAO and makes use of the SNOPT optimizer. Design criteria for the optimization was set up to be the two input mass flows (air and propylene glycol water 30 percent) and the height, width and length of the heat exchanger. Input air temperatures and pressures are based on a hot standard day (+315 K). Constraints for system components were defined relative to the fluid temperature and depend on the limits for the load to be cooled or limits on the fluid itself, as summarized in Table 1, where input temperature means it is a limit on the temperature entering the load and output temperature is a limit on the temperature exiting the load. These limits are based on References 13 and 26. Limits marked as N/A were not considered for these studies. Additional optimization constraints were added on heat exchanger effectiveness and dPqP values to keep them within physical limits and to help optimization stability.

TABLE 1.—ELECTRIC COMPONENT AND COOLING FLUID TEMPERATURE LIMITS IN KELVIN

	Maximum temperature, K	Minimum temperature, K	Maximum input temperature, K	Maximum output temperature, K
Rectifier or Inverter	N/A	N/A	327	344
Motor	N/A	N/A	380	N/A
Propylene glycol 30%	380	310	N/A	N/A
Engine oil	422	350	N/A	N/A

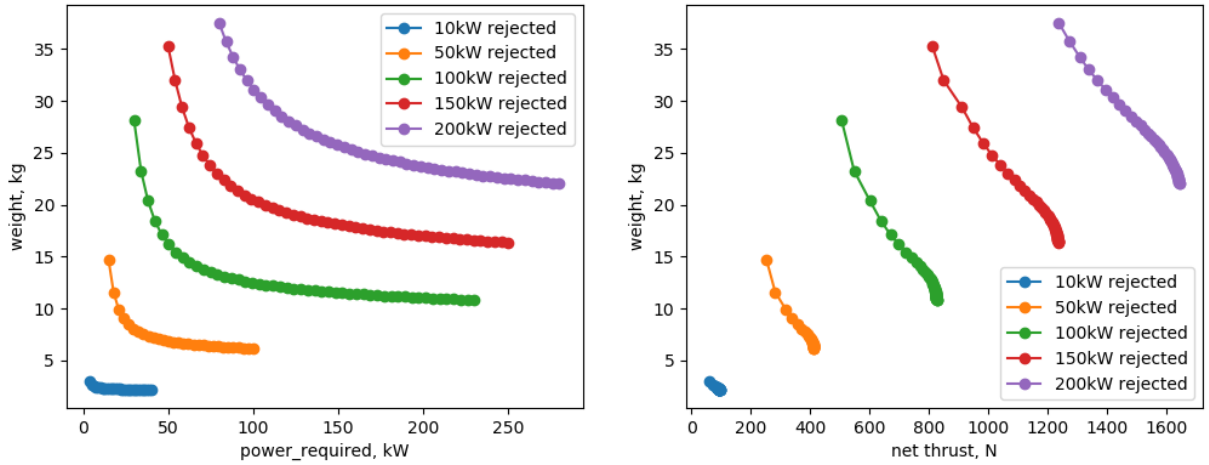

Figure 13.—Pareto fronts of heat exchanger system optimized to different power rejection levels for weight and required power for rectifier cooling (sea level static).

To gain an understanding of the design space, a set of Pareto fronts were generated for several different power rejection levels (10, 50, 100, and 200 kW), with operating conditions consistent with sea level static and temperatures consistent with the cooling of a rectifier (temperatures of 315, 327, and 344 K for air, coolant cold temperature and coolant hot temperature, respectively). For this simulation, it was assumed the system would require puller fans to move air through the HEx. This results in power usage and thrust being directly linked, therefore it was decided to optimize power usage and weight only for the simulation. Results of this analysis, which are shown in Figure 13 show L-curve forms, with the elbow of each curve forming a fairly linear trend. These are due to the larger heat exchangers required to reduce pressure drop for the larger required mass flows. When plotted against net thrust, it can be seen that higher thrust levels correlate with an increase in rejected power. This is because a larger heat exchanger produces less of a pressure drop, which reduces how hard the puller fan has to work. At higher thrust levels of a particular rejected power, it can be observed that there is a falling off of thrust. This leveling off is due to the optimization reaching a point where power rejected is maximized and effectiveness is fairly constant. This leads to air mass flows that are fairly constant, which causes flattening out of the thrust.

In addition, Pareto fronts were generated for changes in air temperature, which would reflect a system that would be designed for higher altitude operation. Air temperature was adjusted in steps of 20 K with rejected power held constant at 50 kW, as shown in Figure 14 (a temperature of 315 K also shown for reference). Here it can be seen that the rejected power L-curve form remains consistent with those previously developed, however weight and required power increase exponentially as the difference in temperature between the coolant and the air is reduced. Note that coolant temperature remained constant for each optimization: 344 K at the inlet of the HEx and 327 K at the exit. Thrust also follows a similar trend with increasing temperature difference.

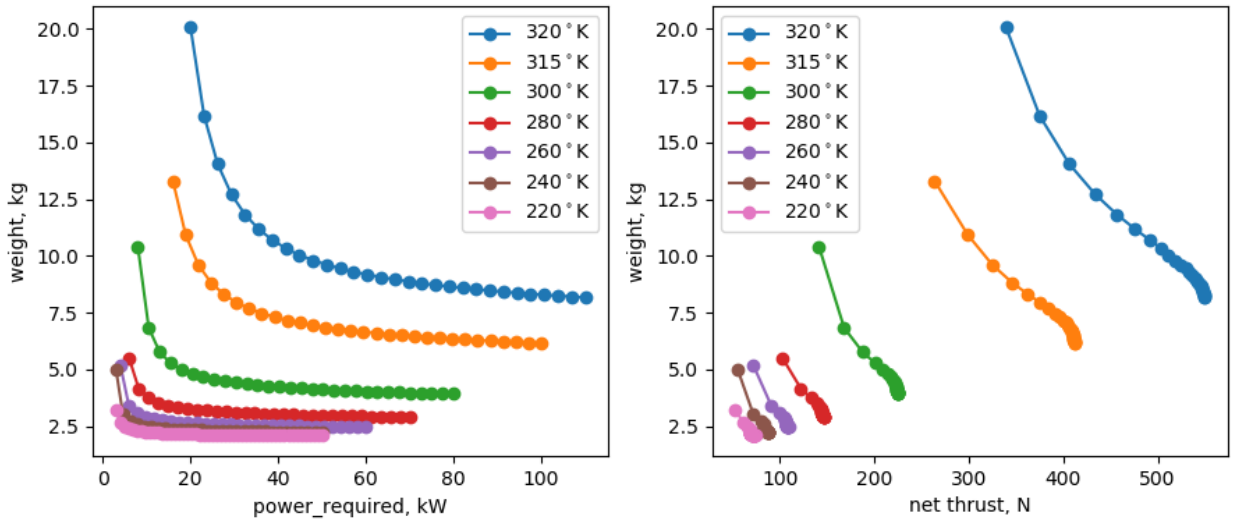

Figure 14.—Pareto fronts of heat exchanger system optimized at different input air temperatures for weight and required power (sea level static, 50 kW power rejection).

To obtain a final design, the system must be optimized to a single point. For this an objective function must be created that takes the metrics and converts them into a value that can be minimized. The objective function used in this paper was modified from a generic aircraft design objective, obtained from Reference 26. This objective quantifies fuel burn as a function of design metrics as shown in Equation (23), where *Wt* is in kg, Pwr is in kW, NetThrust is in N, and Objective is in kg/s. The generic aircraft objective was modified for a tiltwing type aircraft by reducing the power weighting by 90 percent and thrust by 99 percent, which reflects the hover requirement. This relationship is notional for this mission. To gain a real understanding of these relationships, a vehicle optimization (ideally including the TMS) should be run to determine these sensitivities.

$$\text{Objective}_{\text{fuel burn}} = 0.146 * Wt + 0.0887 * \text{Pwr}_{\text{required}} - 0.000248 * \text{NetThrust} \tag{23}$$

Running optimizations at power rejected levels and air inlet temperatures and using the objective in Equation (23), direct relationships are developed, as presented in Figure 15. Here, gains are compared with rejected power and the normalized temperature difference between the air and coolant. Looking at the values obtained and comparing them with the previous Pareto fronts, it is apparent that the objective favors a larger relative weight over required power option. Curve fits for these points were generated and are shown in Equation (24), where polynomial fits all achieve an R^2 value of over 0.99. These curve fits show that weight, net thrust and required power follow a linear trend with respect to rejected power. Normalized temperature difference was similar for each metric and was fit to a single second order trend. Once the operational space is known and can be accounted for, these types of metamodels can offer a method for quickly determining system metrics without running an optimization. However, they should not be used as a substitute of an optimization because they assume a preference for weight and power. Additionally, similar to the map definition, off design coolant temperatures will introduce some error. It should be noted that these equations were developed using static conditions and operation of these heat exchangers during forward flight or using engine bypass air will introduce a pressure gain at the inlet of the heat exchanger reducing or eliminating puller fan power, thrust, and weight contributions.

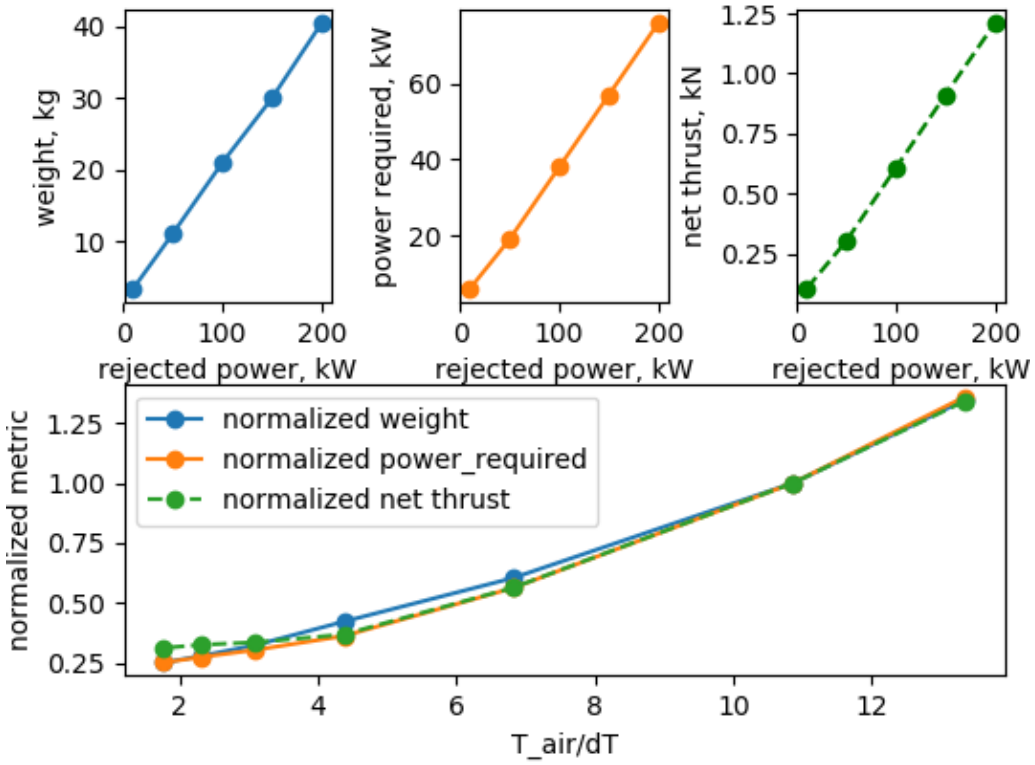

Figure 15.—Weight and power required at various rejected power levels and air temperatures, Note: normalization occurs as the 50 kW design point.

$$
\begin{aligned}
Wt_{\text{uncorrected}} &= 0.194 * \text{Pwr}_{\text{rejected}} + 1.39 \\
\text{Pwr}_{\text{power,required,uncorrected}} &= 0.371 * \text{Pwr}_{\text{rejected}} + 1.33 \\
\text{Fn}_{\text{uncorrected}} &= 5.878 * \text{Pwr}_{\text{rejected}} + 27.58 \\
\text{Normalized Metric} &= 0.0038 * T_{\text{air}}/dT^2 + 0.0352 * T_{\text{air}}/dT + 0.1817
\end{aligned}
\tag{24}
$$

IV. Tiltwing Thermal Management System Modeling and Analysis

Using the above techniques, a TMS was developed for the tiltwing vehicle. For this study, a steady-state TMS was developed at a hover design point (0 MN, 5000 ft) and a transient design was completed running a conservative mission consisting of a 4 min hover followed by a cruise throttle point. The propulsion system architecture for the tiltwing consists of a single turboshaft engine that delivers power to a generator. This generator power is then converted to DC, via a rectifier, and placed on a system bus. The four propellers are each driven by an electric motor that pulls power from the DC bus, with power conditioned by an inverter. The considered TMS was designed to reject heat generated from the engine gearbox (GBX) and electrical system, which consists of a power system generator, rectifier (AC to DC conversion), inverter (DC to AC conversion), and motor. Details of the design are located within Table 2, where component mass was used for transient operation only and was based on a specific power of 7 kW/kg for motors and generators and 16 kW/kg for inverters and rectifiers. The observed temperature limits are listed in Table 1.

TABLE 2.—ELECTRIC MOTOR AND GENERATOR/TURBOSHAFT POWER REQUIREMENTS AND POWER RATINGS

	Hover power, kW	Cruise power, kW	Efficiency,[a] percent	Rejected power at hover, kW	Rejected power at cruise, kW	Assumed mass, kg
Generator	3439	1140	95	181.15	60	571
Rectifier	3269.9	1083	95	172.1	57	210.5
Inverter	768.42	255.74	95	40.44	13.46	38.4
Motor	730	243.2	95	38.42	12.8	104
Gearbox	3625	1210	98	72.5	24.2	Not considered

[a]As taken from Reference 27 for current technology.

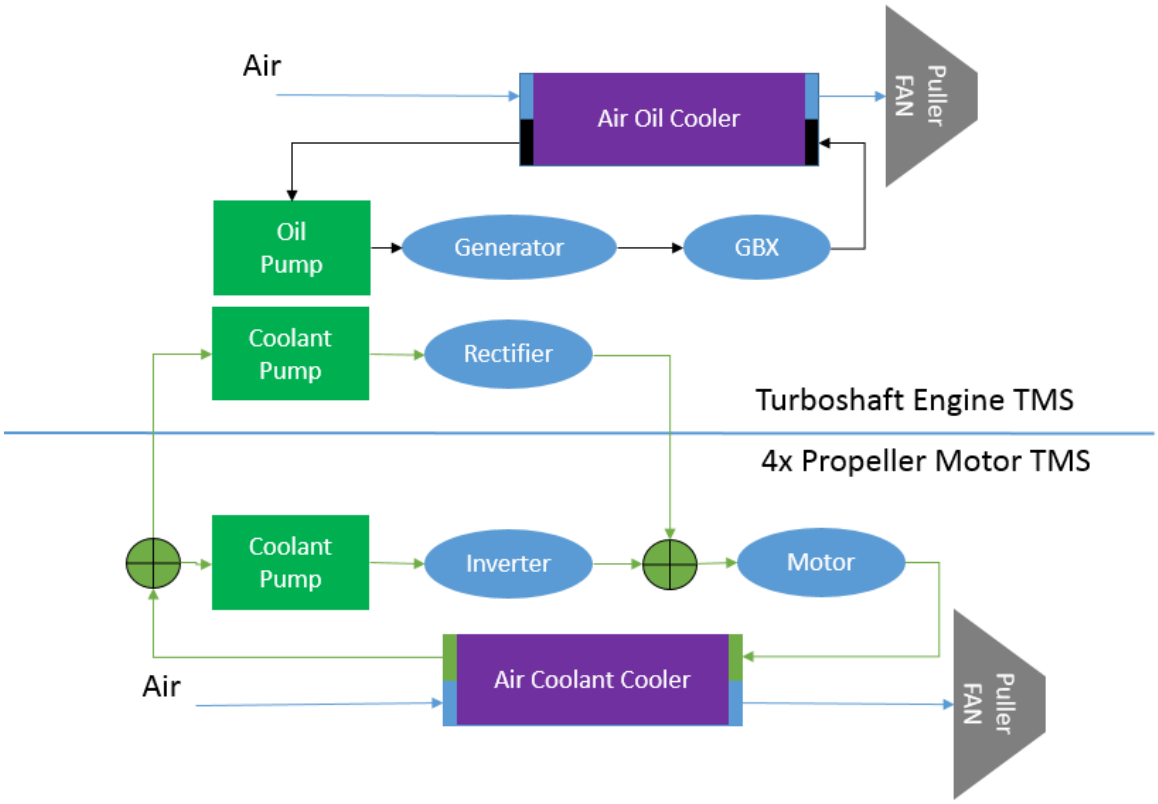

Figure 16.—TMS for 15 passenger tiltwing vehicle.

A diagram of the full TMS system is shown in Figure 16. In this system it was decided there would be an oil and a coolant loop (in this case propylene glycol water 30 percent). Due to their higher operational temperatures, the engine gearbox (GBX) and generator are placed on an oil cooling loop. The four cooling loops for each motor with required power electronics (rectifier and inverter) are placed behind the respective propeller on the wings. A Pareto front was generated for the full tiltwing TMS, as shown in Figure 17, and shows a similar form to the simple Pareto fronts generated in the previous section. Thrust also has a similar form at lower thrust levels, but at high thrust levels the tiltwing Pareto front continues increasing in thrust (the simple systems all became flow saturated and flow dropped off). This is because at low thrust levels the ACC and air oil cooler (AOC) are increasing in air side mass flow. At roughly 5.4 kN net thrust, the air mass flow in the ACC begins to saturate (as in the other AOC simulations above), however the AOC does not saturate and thrust continues to increase as mass flow to it rises.

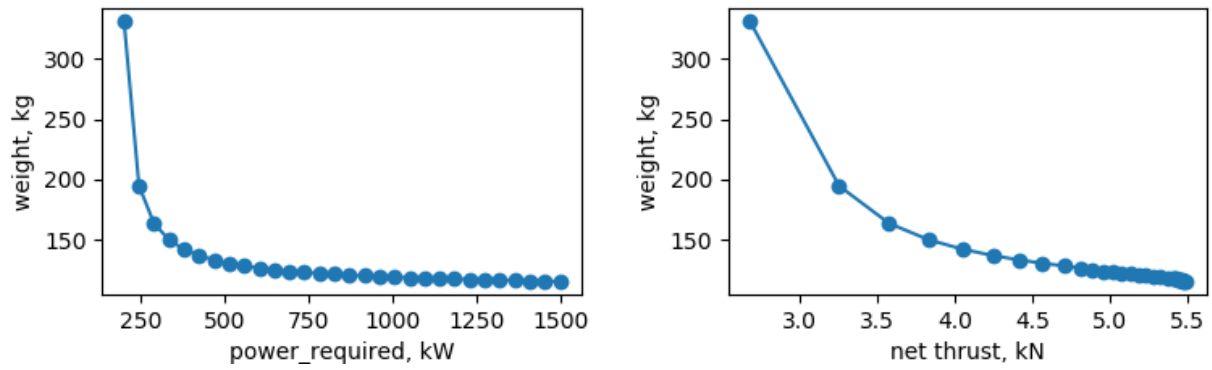

Figure 17.—Pareto front for tilting vehicle.

TABLE 3.—TILTWING TMS MASS FLOW AND TEMPERATURE VALUES

	Fluid	Mass flow through component, kg/s	Input temperature, K	Output temperature, K
Generator	Oil	10.0	[a]380	388
Gearbox (GBX)	Oil	10.0	388	395
Rectifier	Coolant	2.4	[a]327	[a]344
Inverter	Coolant	0.58	[a]327	[a]344
Motor	Coolant	1.18	344	352
Air oil cooler	Air	7.86	318	364
Air oil cooler	Oil	10.0	395	380
Air coolant cooler	Air	6.8	318	336
Air coolant cooler	Coolant	1.18	352	327

[a]Maximum temperature limits

To obtain a final design for the tiltwing TMS, the TMS objective define above (Eq. (23)) was utilized to relate weight, thrust, and required power to aircraft fuel consumption. During optimization this objective would be minimized based on temperature limit constraints.

For this study, two optimizations were run: steady-state and transient. The steady-state optimization was run at a hover design point and assumes static conditions at 5000 ft. Similarly, the transient optimization sizes the TMS for a conservative 4 min hover. For each simulation, it is assumed the TMS designed for a hover condition would be adequate to cooling cruise operation, because cruise requires roughly 1/3 the power as hover. System temperatures and mass flows are shown in Table 3, where it can be seen that the coolant loop is rectifier/inverter exit temperature limited. The oil loop is not temperature limited. In this case, it was more advantageous to increase oil mass flow, which increases heat exchanger effectiveness, than to increase the already large oil to air temperature difference to maximum. This balance is a result of air being relatively expensive (in terms of fuel burn) due to the weight and power required to run the puller fans and shows the heat exchanger is operating in the high coolant region. If the objective multiplier on the required power is reduced, the oil temperature on the output of the gearbox and the air mass flow will rise and heat exchanger effectiveness and weight will be reduced.

Metrics for the optimized system are summarized in Table 4. Here it can be seen that the optimized result using the objective function results in a system that favors a heavier weight with low required power as shown on Figure 17. It can also be seen that the main contributors to the weight are from both AOC and ACC heat exchangers and the oil line due to the large mass flow. In addition one can observe the required power for the pumps is much less than that needed for the puller fans.

Using the correlations developed to estimate these metrics in the last section (metric maps/ metamodel, Eq. (24)) the same metrics are calculated then compared against the more complicated model run in this section. Data from this analysis are shown in Table 5. It should be noted that both models are compared without cooling lines, as the metamodel would not be able to take these into account. From this table it can be observed that weight, required power, and thrust deviate between the models by 13, 8, and 22 percent. These differences are mainly due to differences in model make up, as the metamodel considers only a single type of heat exchanger using a single type of coolant, whereas the physics-based model considers a fairly complex system consisting of many loads, cooling fluids, and heat exchangers. However, this comparison also shows that a metamodel offers a simplified trend that may be used for insight into the system before an optimization is run.

For a final analysis, the full design was optimized transiently. The transient considered was a 4 min hover from hot day rest. This example is notional because worst case conditions could occur during a failure or at a different point along the mission. The purpose of this simulation is mainly to demonstrate how designing the system while taking transients into consideration may or may not influence the design. To update the steady-state model to run transiently, lump masses were added for each of the components (Table 2) along with coolant and oil reservoirs. Their reservoirs act to slow thermal transients, which leads to a potential benefit of sizing at these lower temperatures. The dynamic optimization was set to adjust the size of oil and coolant reservoirs as well as the mass flows and heat exchanger sizes, within the constraints detailed in Table 1. Traces of the system temperatures for the optimized system are shown in Figure 18. In these traces, dashed lines are temperature limits and solid lines are temperatures at the exit

TABLE 4.—TILTWING TMS METRICS

	Quantity	Weight, kg	Power required, kW	Thrust, kN
Air oil cooler	1	27.13	0	0
Oil loop puller fan	1	3.69	95.5	0.8
Oil pump	1	2.8	0.2	0
Oil line	1	15.1	0	0
Air coolant cooler	4	25.3	0	0
Coolant loop puller fan	4	3.22	44	0.6
Coolant loop pump	1	2.4	0.01	0
Coolant loop line	1	11	0	0
Total	-	176.2	271.7	3.2

TABLE 5.—TILTWING TMS PHYSICS BASED MODEL VS. METAMODEL

	T_air into HEx, K	T_coolant into HEx, K	Weight without cooling lines, kg	Required power, kW	Thrust, kN
Metamodel	318	352	131	250.7	3.9
Physics based model	318	Varies	150.1	271	3.2
Difference %	----	-------	12.7%	7.7%	–21.9%

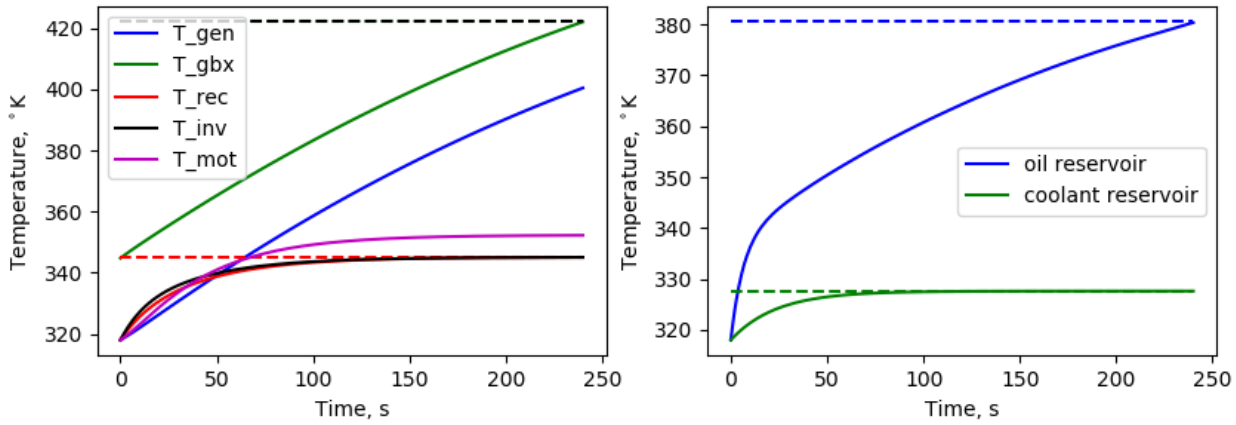

Figure 18.—Trace for dynamic optimization of tiltwing TMS.

of the component. Mass flow from the coolant and oil reservoirs flow offers the coldest temperatures in the system. The reservoirs are then used as the input flow to the rectifier, inverters (coolant loop), and the generator (oil loop). In Figure 18 it can be seen that motor, inverter, and rectifier temperatures hit steady-state around 100 s, while the generator temperature increases more slowly and rises during the entire transient. Mass flow exiting the rectifier and inverters both hit component temperature limits (344 K) and the mass flow exiting the gearbox hits the oil max temperature limit of 422 K. Oil and coolant reservoirs bot hit maximum temperatures for component inputs (327 and 380 K) with the coolant reservoir hitting steady state at about 75 s. The oil reservoir does not hit steady state, with an initial fast transient caused by the gearbox power (gearbox has no state associated with it) and the slower transient caused by the large generator mass. It should be noted that the optimization always selected reservoirs to be sized to the minimum value limit, which was set for simulation stability. This observation generally means that reservoirs are not viable for this mission because the weight increase with the introduction of a cooling fluid reservoir are greater than the weight savings of a design that makes use of the cooler temperatures. It could be that with shorter mission lengths and/or a different arrangement of loads they could be viable.

A metric comparison between the steady-state and transient model is shown in Table 6. Here it shows that the overall TMS has reduced in weight, required power, and thrust, by 2.5, 5.2, and 3.75 percent, when designed for the 4 min hover transient. However, this is not a very fair comparison, as each of the four cooling loops reached steady state well before the end of the transient, therefore, their design was not affected. Considering only the oil cooling loop without the cooling line, as shown in Table 7, it can be seen that this loop was reduced by roughly 14 percent in each metric. This study shows that when deciding to include transients within a design optimization it is important to understand the mission. If different phases of a mission are long and the components are small, then a transient analysis may not be necessary. If the phases are short and components are large (such as large generators or batteries), exploring the system transients may offer a benefit to the design. This transient space may be explored further by introducing options such as starting cooling at a predefined point in the mission or pre-chilling the coolants or a component mass.

TABLE 6.—TILTWING TMS STEADY-STATE MODEL VS. TRANSIENT MODEL

	Weight, kg	Required power, kW	Thrust, kN
Steady-state design	176.2	271.7	3.2
Transient design	171.63	257.6	3.08
Difference %	2.5%	5.2%	3.75%

TABLE 7.—TILTWING TMS STEADY-STATE MODEL VS. TRANSIENT MODEL ONLY CONSIDERING THE OIL LOOP

	Weight, kg	Required power, kW	Thrust, kN
Steady-state design	32.9	95.5	0.8
Transient design	28.33	81.6	0.68
Difference %	13.8%	14.1%	14.0%

V. Summary

This paper details development of a set of equations to be used for the design of an aircraft thermal management system (TMS), performs a set of simple heat exchanger studies, and applies them to a tiltwing turboelectric vehicle. With the increased interest of hybrid or fully electric aircraft, the TMS will become an ever more important aspect of aircraft design. The developed methods detail how a design may be optimized in order to minimize an objective function that takes into account TMS drag, weight, and power usage. System analysis of a simple single load and single heat exchanger show how heat exchanger components operate, how rejected power and input temperatures can affect the design, and details comparisons of several simplified modeling techniques. These comparisons show that the lower fidelity (UA and q/dT map based) modeling techniques studied in this paper incurred differences under 10 percent with the higher fidelity modeling technique as input temperatures deviated from the design point. In addition, system transient behavior is analyzed using a variety of fluid and component masses. Traces of the results are compared against a hypothetical mission show when transient simulation would be required for a particular TMS. Optimization of a full TMS for a 15 passenger tiltwing shows how the full design changes with shifting objectives and gives an estimate of TMS system component weights, power usage, and drag/ net thrust. The optimized design is compared with a simple metamodel with differences under 22 and as low as 8 percent. A steady-state and transient tiltwing design are then compared highlighting potential savings (14 percent weight of the oil loop) of using transient methods for this design.

Appendix—Heat Exchanger Performance

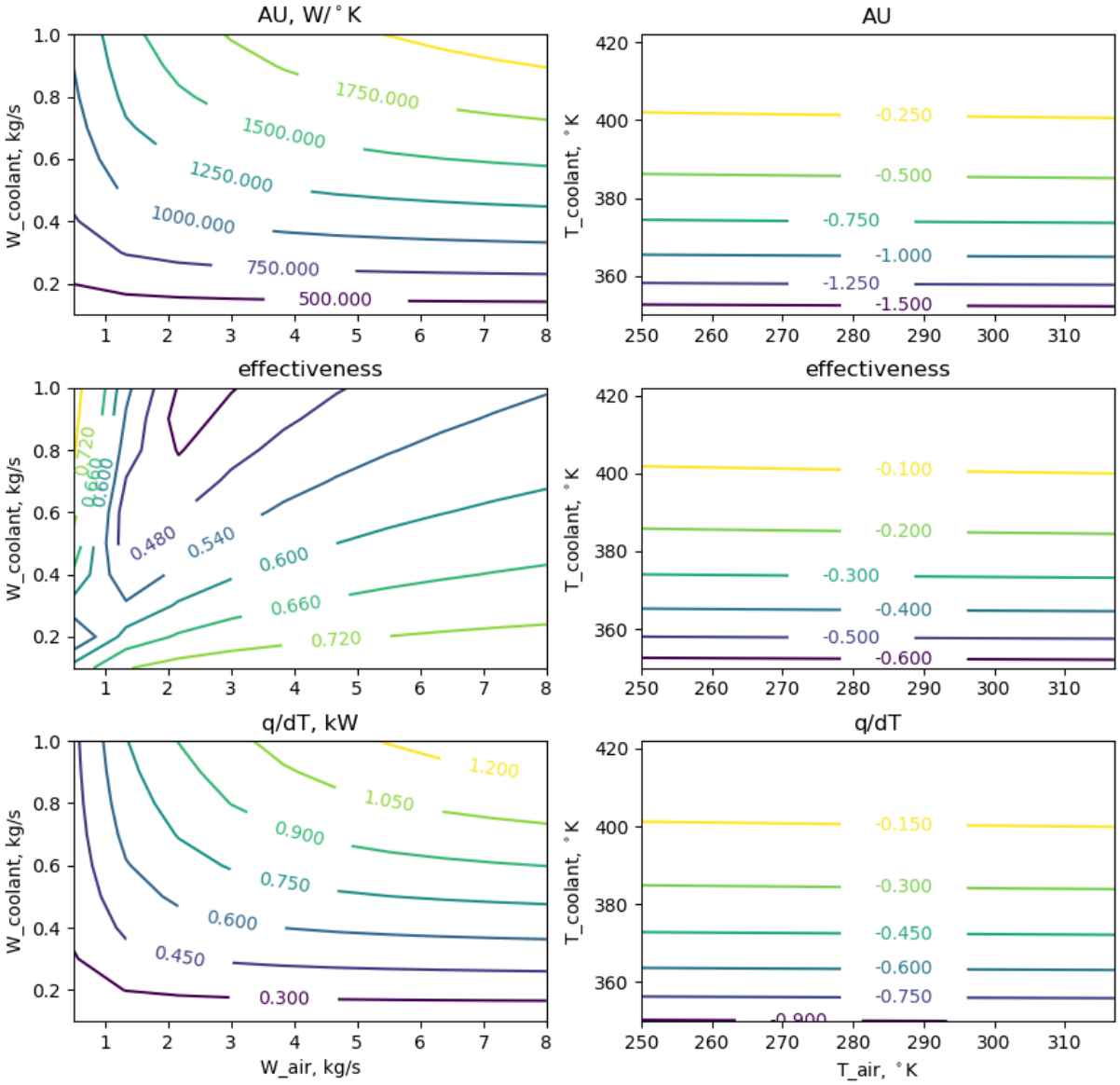

Figure 19.—Heat exchanger performance data as function of input mass flow and normalized delta heat exchanger performance as function of input temperature, at a 50 kW design point and using oil as a coolant.

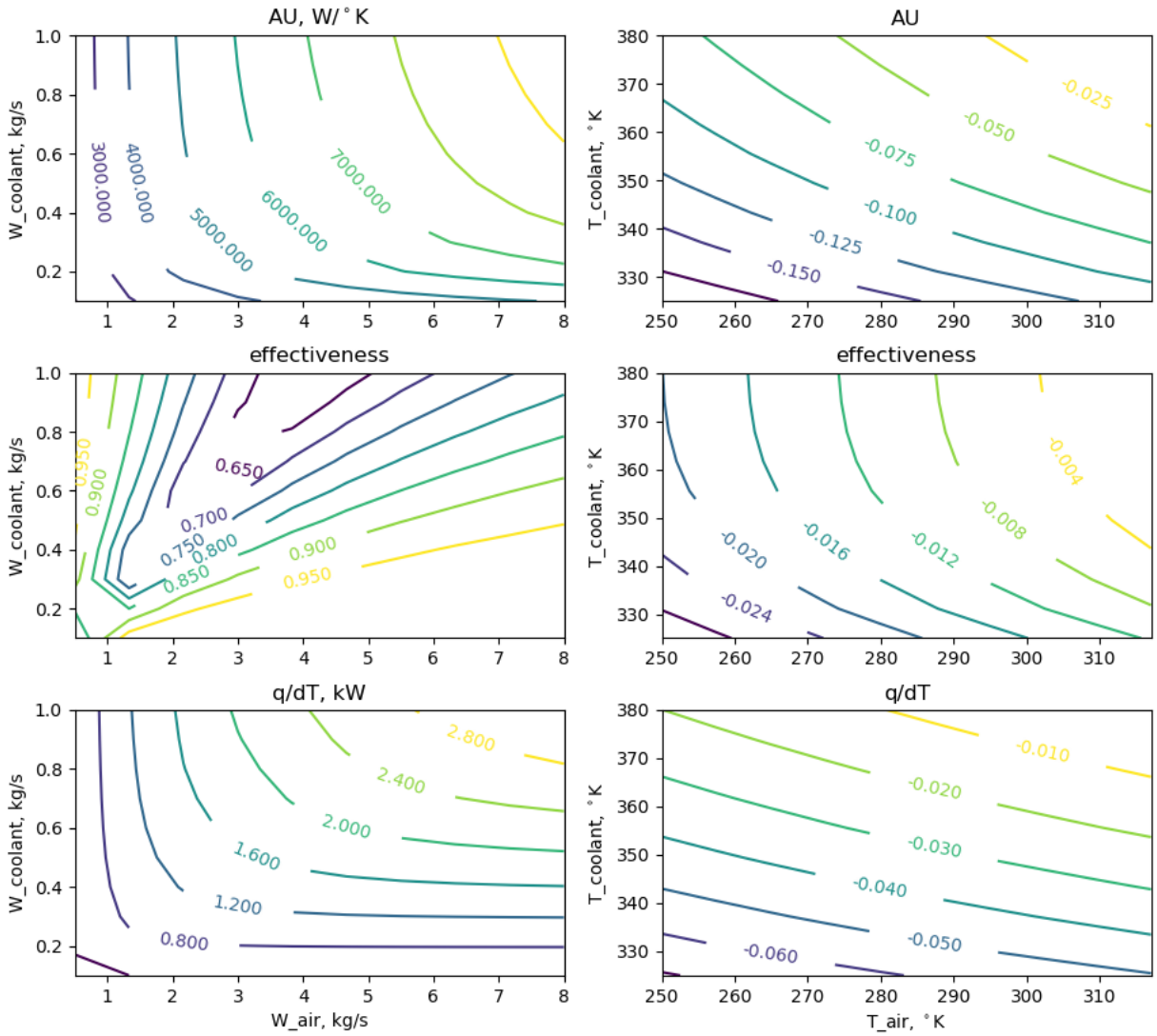

Figure 20.—Heat exchanger performance data as function of input mass flow and normalized delta heat exchanger performance as function of input temperature, at a 150 kW design point using propylene glycol water 30 percent as a coolant.

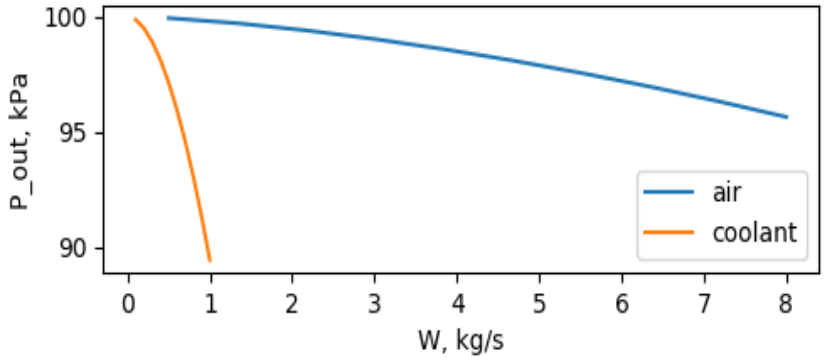

Figure 21.—Heat exchanger pressure as function of input mass flow, at a 150 kW design point using propylene glycol water 30 percent as a coolant.

References

1. Lawson, C.P., Pointon, J.M., "Thermal Management of Electromechanical Actuation on an All-Electric Aircraft," 26th International Congress of the Aeronautical Sciencies, Anchorage, AL, Sept. 14–19, 2008.
2. Bradley, M.K., Droney, C.K., "Subsonic Ultra Green Aircraft Research: Phase II – Volume II – Hybrid Electric Design Exploration," NASA/CR—2015-218704/Volume II, April, 2015.
3. Borer, N.K., Patterson, M.D., Viken, J.K., Moore, M.D., Bevirt, J., Stoll, A.M., and Gibson, A.R., "Design and Performance of the NASA SCEPTOR Distributed Electric Propulsion Flight Demonstrator," 16th AIAA Aviation Technology, Integration, and Operations Conference, AIAA Aviation, American Institute of Aeronautics and Astronautics, Jun 2016.
4. Gieras, J.F., "Multimegawatt Synchronous Generators for Airborne Applications: a Review," IEEE International Electric Machines & Drives Conference, Chicago, IL, May 12–15, 2013.
5. Gieras, J.F., "*Advancements in Electric Machines*," Springer, Jan., 2008.
6. Ganev, E. and Koerner, M., "Power and Thermal Management for Future Aircraft," SAE Technical Paper 2013-01-2273, 2013.
7. Schnulo, S.L., Chin, J.C., Smith, A.D., "Steady State Thermal Analysis of SCEPTER X-57 Wingtip Propulsion," AIAA AVIATION Forum, AIAA 2017-3783, Denver, CO, June 5–9, 2017.
8. Hendricks, E., Aretskin-Hariton, E., Chapman, J., Gray, J., Falck, R., "Propulsion System Optimization for a Turboelectric Tiltwing Urban Air Mobility Aircraft," International Society for Air Breathing Engines, ISABE-2019-24365, 2019.
9. Aretskin-Hariton, E., Lizcano, M., Hurst, J., Hendricks, E., Chapman, J., Goretski, A., "Electrical Cable Design for Urban Air Mobility," to be presented at the AIAA Science and Technology Forum (SciTech), 2020.
10. Aretskin-Hariton, E., Hendricks, E., Ingrahm, D., Chapman, J., Falck, R., Gray, J., Schnulo, S., Chin, J., "Multidisciplinary Optimization of a Turboelectric Tiltwing Urban Air Mobility Aircraft with Thermal and Acoustic Considerations," To be presented at the AIAA Science and Technology Forum (SciTech), 2020.
11. Lents, C.E., Hardin, L.W., Rheaume, J.M, and Kohlman, L., "Parallel Hybrid Gas-Electric Geared Turbofan Engine Conceptual Design and Benefits Analysis," 52nd AIAA/SAE/ASEE Joint Propulsion Conference, Salt Lake City, UT, 2016.
12. Johnson, W., Silva, C., Solis, E., "Concept Vehicles for VTOL Air Taxi Operations," AHS Technical Conference on Aeromechanics Design for Transformative Vertical Flight, San Francisco, CA, Jan. 16–19, 2018.
13. Rheaume, J., Lents, C., "Design and Simulation of a Commercial Hybrid Electric Aircraft Thermal Management System," AIAA/IEEE Electric Aircraft Technologies Symposium, AIAA 2018-4994, Cincinnati, OH, July, 9–11, 2018.
14. Gray, J., Moore, K.T., Naylor, B.A., "OpenMDAO: An Open Source Framework for Multidisciplinary Analysis and Optimization." 13th AIAA/ISSMO Multidisciplinary Analysis and Optimization Conference, AIAA Aviation Forum, AIAA 2010-9101, Fort Worth, TX, Sept. 13–15, 2010.
15. Gill, P., Murray, W., Saunders, M., Wong, E., "SNOPT 7.7 User's Manual," CCoM Technical Report 18-1, Center for Computational Mathematics, University of California, San Diego.
16. R.D. Falck and J.S. Gray, "Optimal Control within the Context of Multidisciplinary Design, Analysis, and Optimization," AIAA Scitech 2019 Forum, San Diego, AIAA 2019-0976, CA, 2019.

17. Kays, W.M., London, A.L., *Compact Heat Exchangers*, 3rd Ed., Krieger Publishing Co., Malabar, Florida, 1984.
18. Incropera, DeWitt, Bergman, Lavine, *Fundamentals of Heat and Mass Transfer*, 6th Ed., John Wiley & Sons, New York, NY, 2002.
19. Cengel, Y.A., *Introduction to Thermodynamics and Heat Transfer*, McGraw-Hill Companies, Inc., 1997.
20. Hearn, T., Hendricks, E., Chin, J., Gray, J., Moore, K., "Optimization of a Turbine Engine Cycle Analysis with Analytic Derivatives," 17th AIAA/ISSMO Multidisciplinary Analysis and Optimization Conference, AIAA Aviation Forum, AIAA–2016–4297, June 13–17, Washington D.C., 2016.
21. Bell, I., Wronski, J., Quoilin, S., Lemort, V., "Pure and Pseudo-pure Fluid Thermophysical Property Evaluation and the Open-Source Thermophysical Property Library CoolProp," Industrial & Engineering Chemistry Research, vol. 53, number 6, pages 2498–2508, 2014.
22. Dynalene, Available: www.dynalene.com.
23. DOW chemical company, "A Guide to Glycols," 2003. Available: http://msdssearch.dow.com/PublishedLiteratureDOWCOM/dh_091b/0901b8038091b508.pdf?filepath=pro.
24. Coordinating Research Council, "Handbook of Aviation Fuel Properties," Society of Automotive Engineers, ADA132106, 1983.
25. Chapman, J., Lavelle, T., Litt, J., "Practical Techniques for Modeling Gas Turbine Engine Performance," 52nd AIAA/SAE/ASEE Joint Propulsion Conference, Salt Lake City, UT, 2016.
26. O'Connell, T., Haran, K., Lents, C., Bayles, B., "Enabling Technologies & Analysis Methods for More-, Hybrid-, and All-Electric Aircraft," AIAA Propulsion & Energy Forum Short Course, Cincinnati, OH, July 8–11, 2018.
27. National Academy of Science, Engineering, and Medicine, *Commercial Aircraft Propulsion and Energy Systems Research: Reducing Global Carbon Emissions*, Committee on Propulsion and Energy Systems to Reduce Commercial Aviation Carbon Emissions Aeronautics and Space Engineering Board Division on Engineering and Physical Sciences, The National Academies Press, Washington D.C., doi: 10.17226/23490, 2016.